Wireless Tissue Palpation: head characterization to improve tumor detection in soft tissue

Marco Beccani[a,*], Christian Di Natali[a], Claire E. Benjamin[a], Charreau S. Bell[a], Nathan E. Hall[a], Pietro Valdastri.[a]

[a]*STORM Lab, Department of Mechanical Engineering, Vanderbilt University, Nashville, TN 37235-1592, USA*

Abstract

For surgeons performing open procedures, the sense of touch is a valuable tool to directly access buried structures and organs, to identify their margins, detect tumors, and prevent undesired cuts. Minimally invasive surgical procedures provide great benefits for patients; however, they hinder the surgeon's ability to directly manipulate the tissue. In our previous work, we developed a Wireless Palpation Probe (WPP) to restore tissue palpation in Minimally Invasive Surgery (MIS) by creating a real-time stiffness distribution map of the target tissue. The WPP takes advantage of a field-based magnetic localization algorithm to measure its position, orientation, and tissue indentation depth, in addition to a barometric sensor measuring indentation tissue pressure. However, deformations of both the tissue and the silicone material used to cover the pressure sensors introduce detrimental nonlinearities in sensor measurements. In this work, we calibrated and characterized different diameter WPP heads with a new design allowing exchangeability and disposability of the probe head. Benchtop trials showed that this method can effectively reduce error in sensor pressure measurements up to 5 % with respect to the reference sensor. Furthermore, we studied the effect of the head diameter on the devices spatial resolution in detecting tumor simulators embedded into silicone phantoms. Overall, the results showed a tumor detection rate over 90 %, independent of the head diameter, when an indentation depth of at 5 mm is applied on the tissue simulator.

Keywords: Pressure sensor, tissue palpation, minimally invasive surgery (MIS), force feedback, tumor localization, surgical robotics.

1. Introduction

During open procedures, surgeons have direct access to soft tissue and organs and use their touch sensation to guide tissue exploration and manipulation. Through tissue palpation, surgeons identify organ margins and features as well as buried structures, such as nerves or arteries, and prevent undesired cuts to healthy tissue. Furthermore, tactile feedback is widely used to gather other valuable tissue information, such as its stiffness, to evaluate the health of the tissue. Tumorous regions are harder than the surrounding tissue [1, 2], but they cannot be visually detected; thus, tissue palpation is the only available tool to guide their localization during the procedure. In recent years, MIS surgical procedures have become a well-established practice and a preferred approach over open surgeries [3] due to its many advantages. These benefits include shortened recovery time, reduced tissue trauma, less pain and discomfort, improved therapeutic outcome for the patient, and increased cost efficiency for the hospital [4, 5].

Despite these advantages, MIS introduces drawbacks such as impairment of the surgeon's dexterity due to the use of long, rigid instrument shafts, reduction of visual feedback, and the impossibility of directly manipulating tissues. This latter shortcoming is one of the main limitations of MIS [6]. In fact, this leads to the exertion of excessive forces, which can cause unintentional damage and stress to healthy tissues [7, 8] or an accidental cut of blood vessels or nerves [9]. Further, MIS removes the physician's ability to sense the location of tumors within the tissue; accurate localization of tumors is essential as it minimizes the resected healthy tissue area while eliminating positive surgical margins created by leaving part of the cancer insite.

Consequently, restoring the sense of touch in MIS has been an active research topic over the last three decades [10, 11] resulting in many devices developed [12] thus far that explore tactile transduction techniques such as resistive, inductive, capacitive, optical, magnetic, piezoelectric, and acoustic [13]. The choice and the placement of the sensing elements is an important matter that can greatly influence the quality of force measurement. Because the effects of forces are transferred through mechanical linkages, the effects of friction, backlash, gravity, and inertia are factors that must be taken into account when high measurement accuracy is needed. Therefore, sensors should be located close to the generation of the forces. When sensors are

*Corresponding author, *E-mail address*: marco.beccani@vanderbilt.edu

embedded in intra-body devices, they are particularly sensitive to heat, noise, water, and tissue. Furthermore, they have fragile structures composed of thin, rigid layers that can break easily when subjected to mechanical stresses. Depending on the application, sensors are sometimes covered with elastomer-based silicone rubbers [14] to guarantee protection against these damaging elements.

While the silicone polymer rubber offers functional sensor-covering protection, it can severely impact the underlying sensor measuring properties. The elastic layer acts as spatial low-pass filter [15] which leads to mechanical cross-talk between neighboring sensor elements; or, in the case of a single sensor, affects the stress distribution under the covering. Additionally, the rubber affects the measurements by introducing hysteresis effects, which are due to the rubber's viscoelasticity, and nonlinear behaviors which lead to undesired responses and significant loss of pressure data [16]. Furthermore, current tactile systems for MIS have a rigid shaft and require a dedicated entry port, both of which limit the systems maneuverability and use in a clinical context. Thus, despite the many efforts of the research community, the development of satisfactory tactile sensors have not yet been realized nor adopted in a clinical context [13, 12, 16]

In [17], a WPP is presented to restore tissue palpation in MIS by creating a real-time stiffness distribution map of the palpated tissue. The WPP utilizes a field-based magnetic localization algorithm to measure its position, orientation, and tissue indentation depth in addition to pressure-sensing data from a barometric pressure sensor covered by silicone rubber [18]. During tissue palpation, the WPP head is pressed against the compliant tissue, causing deformation of both the tissue and the silicone rubber. Despite encouraging preliminary results, the WPP faces a number of challenges. The deformation of both materials introduces nonlinearities which affect the measurements. In addition, the palpation of smaller tissue areas is not possible with the current WPP because of the fixed diameter of the rubber covering. Furthermore, the WPP heads non-disposable rubber covering loses its mechanical properties after multiple uses on tissue. Subjecting the WPP to sliding forces can cause the sensor's rubber cover to detach. This detachment leads to situations in which head replacement is necessary, and the entire probe must be rebuilt.

In this work, we implemented a new calibration methodology to reduce the error introduced by the rubber nonlinearities on the pressure measurements, and thus reconstruct the measured pressure more accurately. The method was verified with different diameter heads fabricated according to a new design that allows for exchangeability and disposability of the WPP heads. Finally, we studied the effect of the mounted head diameter on the device's ability to detect different size lumps embedded into the silicone. Although this work used a specific probe (*i.e.*, the WPP), the contribution of the calibration procedure described in this paper can be generalized to any probing system in which silicone rubber is interposed between the target tissue and the mechanical sensor.

This paper is organized as follows: Section 2 describes the WPP head design and its fabrication procedure, Section 3 presents the theory behind the calibration of the head, Section 4 explains the assessment platform for calibration and presents the results of the calibration method. Section 5 reports the ability of the WPP head to detect different sized lumps embedded at various depths in silicone phantoms, and finally, Section 6 discusses conclusions and future works.

2. WPP head design and fabrication

A number of goals and constraints were considered during the design of the WPP head. The diameter of the WPP must not exceed 12 mm, the maximum size for insertion through a surgical trocar (*e.g.*, the 5-12 Vesaport Plus, Covidien, USA has a diameter of 13 mm). Exchangeability of the heads is desirable for the probe so that geometric features of the rubber, such as diameter and thickness, can be varied and implemented according to the region to be palpated. This feature enables easy replacement of the heads, useful because the silicone rubber is the most fragile part of the device and because the heads can therefore be treated as disposable. In this design, the sensor is mounted with its sensitive area exactly in the center of the rubber to guarantee a uniform pressure exerted on the tissue. The head was designed in order to meet all of these constraints. In particular, as represented in Fig. 1(a), all WPP head components were integrated inside a cylindrical plastic shell which was fabricated using rapid prototyping (Objet 30, Objet Geometries LTD, USA) and which mates with the WPP body.

The overall height of the WPP head, including the silicone rubber, is 58.5 mm, and the overall diameter is 12 mm. This part has an inner diameter of 9.9 mm to fit a double-layered circular Printed Circuit Board (PCB) (thickness 1.6 mm). A rectangular opening on the 3D printed surface (length 5 mm, width 3 mm) exposes the barometric pressure sensor (MPL115A1, Freescale, USA), mounted on top of the PCB and covered with the silicone rubber. On the other side of the PCB is a connector (CLP-104-02-G-D, Samtec, USA), which mates with another connector (FTS-104-02-F, Samtec, USA) placed on top of the WPP body on a second PCB (diameter 9.9 mm, thickness 1.6 mm). To keep the sensor aligned in the center of the WPP and to strengthen connection to the body, three aluminum rods (length 15 mm, diameter 1 mm) are inserted through the mating head and both PCBs. The head's flat surface is covered by 3 mm of silicone rubber (Dragonskin 10, Smooth On, USA). The material and thickness were chosen for better performance in terms of resolution, measurement range, and sensitivity as showed in [19].

After initial fabrication, the head was placed in a degassing oven and subjected to the 680 cmHg vacuum pres-

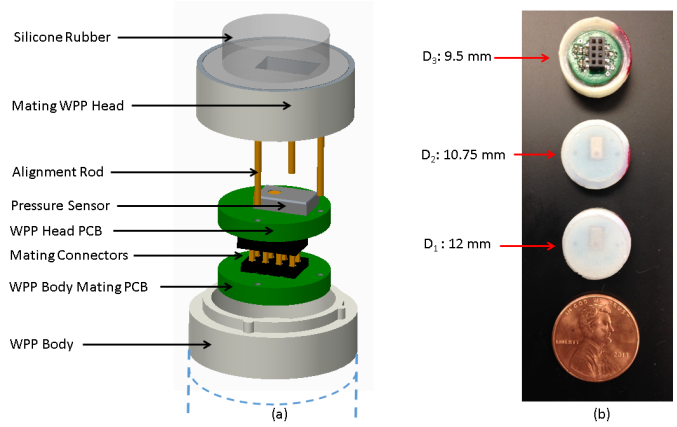

Figure 1: The WPP head explosion view (a), the fabricated heads of different diameters (b).

sure for 2 min and 30 sec (any decrease in the amount of air remaining in the material was negligible after this amount of time). Three different diameters (*i.e.*, $d_1 = 12\ mm$, $d_2 = 10.75\ mm$, and $d_3 = 9.5\ mm$) of material on the head, shown in Fig. 1(b), were chosen to test the effects of the sensing surface area on the device's accuracy and precision during palpation. The quantity of material used for each diameter was 0.50 g, 0.45 g, and 0.40 g, respectively, within a tolerance of 0.01 g.

3. Principle of Operation

3.1. Calibration

Under the hypothesis that the measurements are affected by the rubber nonlinearities, the sensor's calibration requires the measurement of the two quantities: $P_h(t)$, the sensor data, and $P_R(t)$, a known applied pressure used as a reference. As shown in Fig.2(a), if the WPP probe is pressed against a rigid non-deformable material, only the silicone rubber compresses due to $P_R(t)$. In this case, the rubber indentation, $\delta_h(t)$, is equal to $\delta(t)$, the indentation of the WPP at the contact position. The silicone rubber then compresses from H_0, the initial thickness of the rubber, at a certain $\delta_h(t)$, as illustrated in Fig.2(b), depending on the applied pressure $P_R(t)$.

The two pressures $P_R(t)$ and $P_h(t)$ can be expressed at any instant of time as a function of the rubber indentation $\delta_h(t)$. In this case, because the thickness of the silicone rubber is known *a priori*, they are both a function of the strain $\epsilon_h(t)$ of the silicone. In the case that the tissue thickness is unknown, they can be expressed as a function of a pseudo-stiffness variable (kPa/mm). We define $\Phi_h[\epsilon_h(t)]$ and $\Phi_R[\epsilon_h(t)]$ as two interpolating functions of the independent variable $\epsilon_h(t)$, numerically quantified through experimental calibration from $P_R(t)$ and $P_h(t)$, respectively. Their ratio, $H[\epsilon_h(t)] = \frac{\Phi_R[\epsilon_h(t)]}{\Phi_h[\epsilon_h(t)]}$, can be represented by a state-space system filter as:

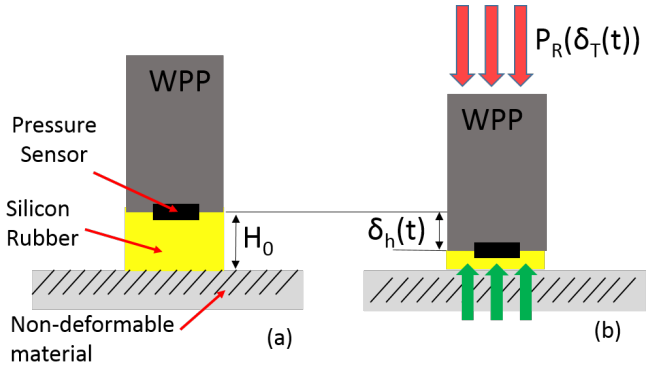

Figure 2: Schematic diagram of the calibration procedure at contact (a) and at an arbitrary instant of time (b) for a non-deformable material.

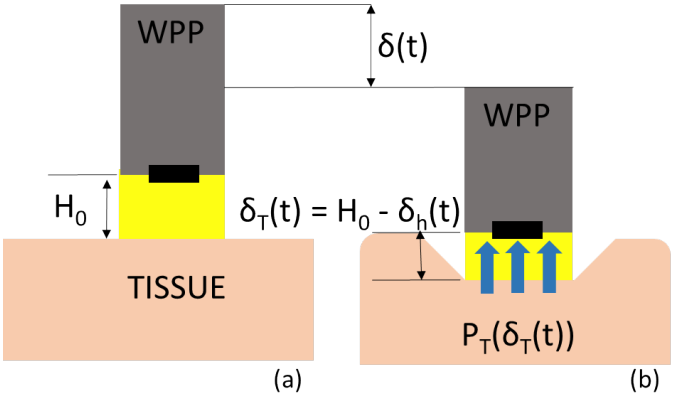

Figure 3: Schematic diagram of the WPP palpating tissue at contact (a) and at an arbitrary instant of time (b) for a deformable material.

$$\begin{aligned} \dot{\mathbf{x}}(t) &= A\mathbf{x}(t) + B\mathbf{P_h}(t) \\ \tilde{\mathbf{P}}_\mathbf{h}(t) &= C\mathbf{x}(t) + D\mathbf{P_h}(t) \end{aligned} \tag{1}$$

The filter terms A, B, C, and D are the matrix, or state-space form, of the filter's difference equations. Specifically, $\mathbf{x}$ is the state vector, $\tilde{\mathbf{P}}_\mathbf{h}$ is the output vector, and $\mathbf{P_h}$ is the input vector. Given the raw sensor measurements, the space-state system filter reconstructs the value of $P_R(t)$.

When the WPP is pressed against tissue, as shown in Fig.3, the silicone rubber is compressed by the quantity $\delta_h(t)$, and the compression of the tissue results in an indentation of $\delta_T(t)$.

The indentation depth $\delta_T(t)$ can be expressed as:

$$\delta_T(t) = \delta(t) - \delta_h(t) \tag{2}$$

where $\delta(t)$ is the longitudinal position of the WPP with respect to the contact point and the quantity $\delta_h(t)$ is the rubber compression[20]. The silicone head compression $\delta_h(t)$ can be evaluated from the raw sensor pressure data

$P_T(t)$ as the head pushes against the tissue. By applying this data to the inverse function Φ_h^{-1} we have:

$$\delta_h(t) = \Phi_h[P_T(t)]^{-1}. \quad (3)$$

Rearranging Eq. 2 and Eq. 3, the tissue indentation $\delta_t(t)$ can be expressed as:

$$\delta_t(t) = \delta(t) - \Phi_h[P_T(t)]^{-1} \quad (4)$$

The derived tissue indentation, $\delta_t(t)$, applied to the analytical function $\Phi_h(\delta_t(t))$ reconstructs the resulting pressure points that the sensor would have measured for the head compression $\delta_t(t)$. The resulting pressure values $\Phi_h(\delta_t(t))$ are then applied as $P_h(t)$ to the state-space system filter to reconstruct the reference pressure $P_R(t)$.

4. Experimental Platform and Calibration Assessment

In this section, we describe the experimental platform and present the trials performed to assess the WPP algorithm.

4.1. Experimental Platform

The experimental platform to assess the WPP head calibration is presented in Fig.4. A 6-axis load cell (NANO17, ATI Industrial Automation, USA) was mounted at the end effector of a six degrees of freedom robotic manipulator (RV6SDL, Mitsubishi Corp., Japan). A rapid prototyping part (Objet 30, Objet Geometries Ltd, USA) was then assembled with the load cell to host the WPP and used during calibration as the reference pressure sensor. The load cell has a resolution of 3.125 mN, and its measurements were collected using a Universal Serial Bus (USB) acquisition board (NI-PCI 6224, National Instruments, USA) at a sampling frequency of 40 kHz. The embedded pressure sensor data was acquired by the WPP microcontroller (CC2530, Texas Instruments, USA) using its Serial Peripheral Interface (SPI). Data was then packaged into a 12-byte payload consisting of a counter, time stamp, and the pressure sensor measurements. In this application, there was no requirement for WPP wireless communication; therefore, the device was tethered and the payload was transmitted to the USB port of a Personal Computer (PC) through a USB serial converter (UM232R, FTDI, UK). Data refresh occurred every 2.2 ms, resulting in a 454 Hz refresh frequency. A multi-threaded C++ application [21] running on the PC (Windows, Microsoft, USA) was implemented to simultaneously acquire $P_h(t)$ from the pressure sensor, $P_R(t)$ from the load cell, and the robot manipulator position. Acquired data was then analyzed using Matlab (Mathworks, USA), where the calibration was implemented. Subsequently, after verifications, the state space filter was embedded in the C++ application with a resulting refresh time of 14 ms $\pm$ 3 ms.

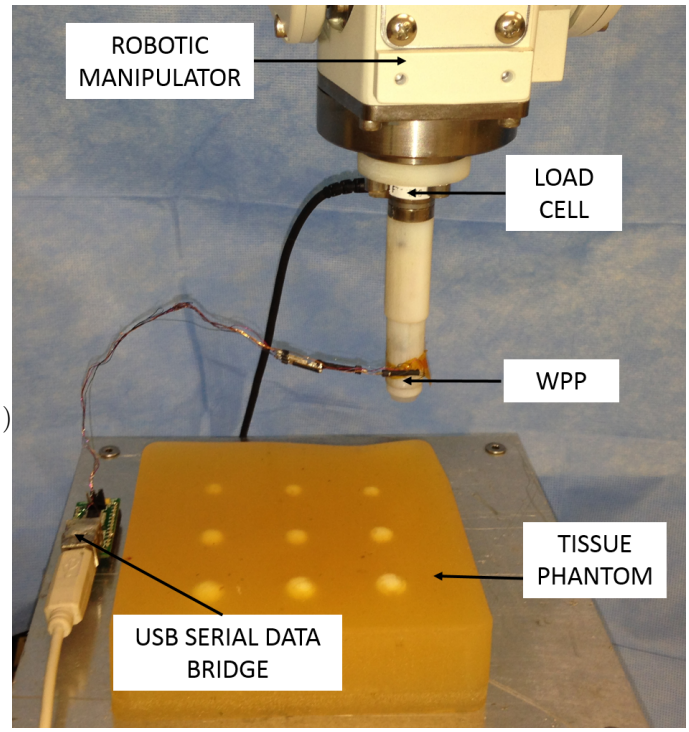

Figure 4: The platform to assess the WPP head calibration.

4.2. Calibration Assessment

The calibration described in Section 3 was then assessed through several different trials. First, the analytical calibration functions for the three different heads were determined. Then, the calibration was validated by applying a dynamic strain to the WPP to ensure that it was not affected by the palpation velocity. Finally, the WPP heads were tested by palpating two silicone samples of different stiffnesses.

4.2.1. Analytical functions calculation

To calibrate the WPP, the numerical functions Φ_h and Φ_R were evaluated by pushing the device against a rigid support and recording both $P_R(t)$ and $P_h(t)$ together with the external manipulator position. The head indentation $\delta_h(t)$ was thus derived as a function of the pressures $P_R(t)$ and $P_h(t)$. The WPP was pushed at a constant speed of 0.3 mm/s starting from the contact position H_0. The trials consisted of five loading/unloading cycles; the measured values were then averaged before being fitted with a fifth order polynomial to minimize the residuals, resulting in $\Phi_h(\delta_h(t))$ and $\Phi_R(\delta_h(t))$ as shown in Equation 5.

$$\begin{aligned} \Phi_h[\delta_h(t)] &= \textstyle\sum_{i=0}^{5} a_i \delta_h(t) \\ \Phi_R[\delta_h(t)] &= \textstyle\sum_{i=0}^{5} a_i \delta_h(t) \end{aligned} \quad (5)$$

The square of the correlation coefficients and the derived polynomial coefficients for the fitting are reported in Table 1.

	$\Phi_R(d_1)$	$\Phi_h(d_1)$	$\Phi_R(d_2)$	$\Phi_h(d_2)$	$\Phi_R(d_3)$	$\Phi_h(d_3)$
R^2	0.9907	0.9902	0.9913	0.9876	0.9974	0.9958
a0 (kPa)	.08	0.34	1.23	2.36	0.42	1.73
a1 ($\frac{kPa}{mm}$)	-12.68	-11.55	-126.41	-258	-22.64	-268.37
a2 ($\frac{kPa}{mm^2}$)	344.62	184.96	$4.81 \cdot 10^4$	$6.9 \cdot 10^3$	$2.87 \cdot 10^3$	$6.98 \cdot 10^3$
a3 ($\frac{kPa}{mm^3}$)	$-1.89 \cdot 10^3$	$-1.46 \cdot 10^3$	$-4.87 \cdot 10^4$	$-7.72 \cdot 10^4$	$-2.11 \cdot 10^4$	$-6.11 \cdot 10^4$
a4 ($\frac{kPa}{mm^4}$)	$5.27 \cdot 10^3$	$5.2 \cdot 10^3$	$2.51 \cdot 10^5$	$4.06 \cdot 10^5$	$9.57 \cdot 10^4$	$-2.84 \cdot 10^5$
a5 ($\frac{kPa}{mm^5}$)	$-4.79 \cdot 10^3$	$-5.09 \cdot 10^3$	$-4.45 \cdot 10^5$	$-6.89 \cdot 10^5$	$-1.39 \cdot 10^5$	$-4 \cdot 10^5$

Table 1: Correlation coefficients R^2 and the polynomial coefficients derived of the fitting.

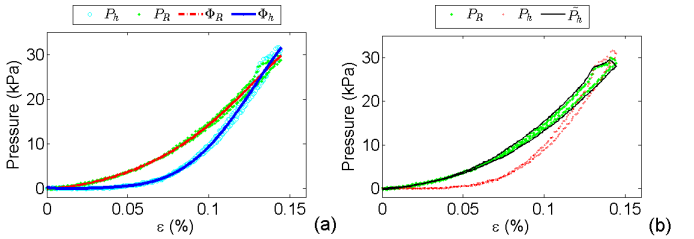

Figure 5: The raw pressure data, the reference pressure, and their numerical functions' interpolations (a), the raw and calibrated pressure data compared with the reference pressure P_R (b).

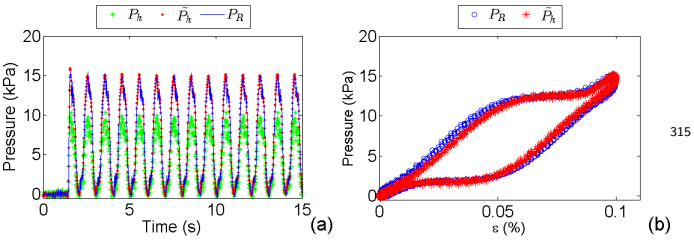

Figure 6: The WPP head is tested under a dynamic strain at a frequency of 1 Hz (a) The results of the stress-strain curve for the loading unloading cycles (b).

In Fig.5(a), the graphs of $P_h(\epsilon_h(t))$, $\Phi_h[\epsilon_h(t)]$, $P_R(\epsilon_h(t))$ and $\Phi_R[\epsilon_h(t)]$ are represented for a single loading/unloading cycle (*i.g.*, $d_2 = 10.75$ mm) where $\epsilon_{\%}$ is the compression of the rubber with resect to its thickness. The data shows that from the contact point (*e.g.*, $\epsilon_{\%} = 0$), the WPP does not respond to the applied pressure until a certain strain is reached (for this head $\epsilon_h(t) = 5$ %). The difference between the two sensors' measurements, as the results show, give evidence as to how the sensor readings are affected by the silicone rubber properties.

Fig.5(b) shows the result of applying $P_h(t)$, the error between the reference, $P_R(t)$, and the system output, to Equation 1. If we do not consider the silicone rubber nonlinearities which cause the sensor inefficient measurements until a value of $\epsilon_h(t) = 5$ % is reached, the relative error is 19 %. The graph shows how with the calibration, $\tilde{P_h}$ follows P_R, and the resulting relative error is equal to 4.25 $\pm$ 0.7 % for the three different diameters.

Figure 7: Palpation of the two different stiffness samples. Unfiltered sensor data (in red) and filtered sensor data (in black)

4.2.2. Dynamic Assessment

The calibration was then validated under a variable speed to verify that the dynamic stress over time did not perturb the system performance. For this purpose, the WPP was moved with a sinusoidal displacement at a frequency of 1 Hz on the rigid surface. This frequency is comparable to clinical usage, in which the WPP is grasped and pushed against tissue with a surgical grasper. For this trial, the silicone rubber was compressed from the contact point to 10 % of its thickness. The trial consisted of 14 loading/unloading cycles, as shown in Fig. 6(a), where the measurements for the reference pressure $P_R(t)$ and both the raw and calibrated sensor data are displayed. The plot shows that the calibration is not affected by the dynamic response of 1 Hz load/unload cycles. In particular, using the data from the load/unload cycles, we can plot the value of the pressure as a function of the strain for each cycle, as represented in Fig 6(b). Based on the experimental results, we can conclude that though the silicone layer embedding the barometric pressure sensor introduces nonlinearities in the sensor response, these effects can be corrected, reducing the relative error of the reference pressure down to 2.1 %.

4.2.3. Tissue samples fabrication

Finally, we tested the WPP ability to detect differing stiffnesses of two synthetic tissue samples. The samples were fabricated by combining two ratios of liquid plastic and hardener (PVC Regular Liquid Plastic and Regular Liquid Plastic Hardener, MF Manufacturing, USA Sample 1: 1 to 5 ratio, Sample 2: 1 to 3 ratio). The samples were 30 mm thick with lateral sides of 100 mm. As in the previous trials, the WPP was mounted on the distal side of the load cell to indent the samples. Five loading/unloading trials reaching an indentation depth of approximately 15 % of the sample thickness were performed for each tissue sample at a constant speed of 1 mm/s.

The stiffnesses measured by the load cell were equal to $E_1 = 43.65$ kPa and $E_2 = 76.63$ kPa, respectively, and for the WPP were $E_{1\ WPP} = 43.18$ kPa, $E_{2\ WPP} =$

75.77 kPa. Experimental plots obtained from a single loading are represented in Fig.7. The results show that the WPP was effective in detecting the stiffness of different samples with an average relative error equal to 1.1 % for the first sample and 2.4 % for the second sample. Overall, with the introduced method the WPP is able to measure the stiffness of different samples with an average relative error below 2%.

5. Tissue abnormality detection by different diameter WPP heads

5.1. Tissue samples palpation validation

Bench experiments were conducted to investigate the efficacy of the WPP in identifying buried lumps of different sizes embedded into tissue phantoms at different depths. These phantoms, PH_1 and PH_2, were constructed similarly to [6] by combining different proportions of liquid plastics and hardener (PVC Regular Liquid Plastic and Regular Liquid Plastic Hardener, MF Manufacturing, USA PH_1: 1 to 5 ratio, PH_2: 1 to 4 ratio). The nine embedded spherical lumps were made using rapid prototyping (Material Elastic modulus 40-60 MPa). The dimensions of the phantoms and the lump locations, dimensions, and depths are shown in Fig. 8(a), Fig. 8(b) and Fig. 8(c).

5.2. Experimental Protocol

The elastic moduli of the two silicone phantoms were measured by conducting multiple indentation tests on the tumor-free areas, and resulted as $PH_1 = 42.78 \pm 1.45$ kPa and $PH_2 = 21.88 \pm 1.78$ kPa. These values are typical for human tissues, as reported in [22]. Uniaxial palpation was performed on both the phantoms with the WPP mounted on the end effector of the robotic manipulator and perpendicular to the phantom's surface. The manipulator was programmed to perform indentations along the phantoms' x-axes at intervals equivalent to half of the head diameter. This created an r by c matrix of indentation points. The number of points for each row was set equal to the number of columns, creating an area of about $90 \times 90\ mm^2$ to be indented with the three WPP diameters. The largest diameter head had $r_{d_1} = c_{d_1} = 16$ row and column combinations, resulting in 16×16 indentation points. The other two heads had $r_{d_2} = c_{d_2} = 18$, and $r_{d_3} = c_{d_3} = 20$ row and column numbers respectively. Placing the origin at the phantom corner, the first indentation point P_0, was set at $x = 25$ mm and y = 25 mm.

The phantom surface is not perfectly even, thus the contact point with the surface needs to be estimated for each of the indented points. Therefore, before the start of the palpation procedure, the standard deviation of the sensor measurements was calculated with no load applied. The WPP then approached the phantom surface from a distance of about 20 mm and a speed of 2 mm/s until the sensor pressure measurement exceeded three times its standard deviation. When this condition was verified, the manipulator z position was assumed to be in contact with the phantom surface. Then, the WPP indented the phantom at a speed of 1 mm/s until the programmed indentation depth was achieved. Motion in the opposite direction with the same speed was performed until the WPP returned to the depth of the contact point. Here, the probe was moved 20 mm up from the surface and then shifted along the phantoms x-axis to the next indentation point. This procedure was repeated c times (equal to the number of columns in the indentation matrix) before the manipulator shifted along the phantoms y-axis to begin a new path. The silicone phantoms were found to have an uneven surface with average surface height along their z-axes of 33 ± 0.57 mm and 33 ± 0.26 mm, respectively.

To evaluate the robustness and repeatability of the probe, indentation palpation trials were repeated five times for each of the different diameter heads with an indentation depth of 3 mm and 5 mm.

5.3. Data Analysis

After completion of the palpation experiments, pressure indentation maps of the two phantoms for the different head and indentation depth combinations were generated. Embedded lumps are stiffer than the surrounding silicone, and their location in the map is represented by a higher stiffness region (red). Figures 9(a) and (c) show the maps obtained from one of the trials by using d_1 mounted on the WPP to palpate PH_1. In this trial, the indentation pressure ranged from 4.75 kPa to 19.5 kPa for the 3 mm indentation depth, and from 19.9 kPa to 60.25 kPa for the 5 mm indentation depth. Figures 10(a) and (c) show the pressure map for PH_1, where the indentation pressure ranged from 1.8 kPa to 12.1 kPa for an indentation depth of 3 mm and from 3.4 kPa to 23.15 kPa for an indentation depth of 5 mm. In both tissue phantoms, the measured stiffer values corresponded to the lumps larger and closer to the surface (*i.e.*, A_1).

To characterize the effectiveness of the different WPP heads in localizing the embedded lumps, a contour map of the indented surface was generated for all the trials. The plot consisted only of the regions where the indentation pressure exceeded a certain threshold, specifically, the sum of the minimum pressure measured by the map and 5 times the sensor standard deviation. Figures 9(b) and (d) and Figures 10(b) and (d) show the resulting contour maps for the same trials. Each individual palpation point is represented by a single point (shown in black), while the spherical embedded lumps are marked by dotted circles (shown in purple) of their actual size.

The effectiveness of the WPP in detecting different size lumps is reported in Table 2 and Table 3 for PH_1 and PH_2, respectively. These tables report the average errors for the trials between the stiffness peaks and the ground truth lumps' center locations along with the average detected lump area for all the trials. Overall, for all trials on both phantoms, the average relative location error in detecting the lumps was equal to E_x=1.4 mm, E_y=1.2 mm

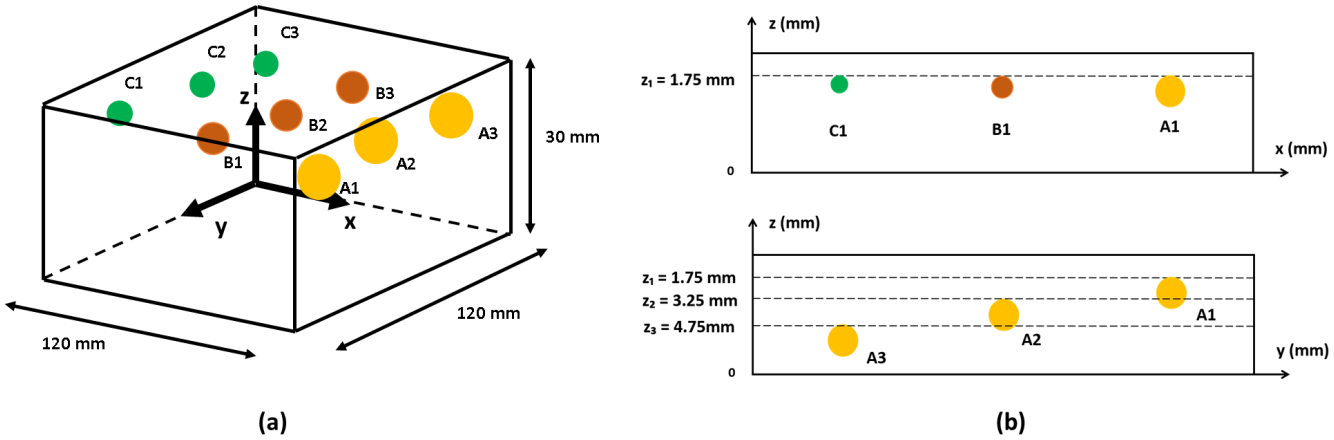

Figure 8: Dimensions of the fabricated phantoms with the embedded lump locations (a) and their relative depth (b).

Phantom 1						
Head Diameter	d_1		d_2		d_3	
Indentation Depth	$\delta = 3$	$\delta = 5$	$\delta = 3$	$\delta = 5$	$\delta = 3$	$\delta = 5$
Embedded Lump	A_1					
$S(mm^2)$	128	121	108	104	89	82
Error (x;y)		(1.7;1.2)		(0.5;1.9)		(1.6;1.5)
Embedded Lump	A_2					
$S(mm^2)$	98	102	97	94	78	85
Error (x;y)		(0.8;0.3)		(0.5;1.3)		(0.3;0.1)
Embedded Lump	A_3					
$S(mm^2)$	92	107	105	107	74	89
Error (x;y)		(1.7;0.1)		(0.4;3.2)		(1.3;3.2)
Embedded Lump	B_1					
$S(mm^2)$	71	74	63	69	54	61
Error (x;y)		(1.2;0.8)		(2.2;1.4)		(0.2;0.3)
Embedded Lump	B_2					
$S(mm^2)$	58	67	52	61	57	64
Error (x;y)		(1.5;1.1)		(1.2;1.5)		(1.4;2.2)
Embedded Lump	B_3					
$S(mm^2)$	51	65	54	57	58	60
Error (x;y)		(1.2;1.1)		(3.2;2.9)		(1.3;1.4)
Embedded Lump	C_1					
$S(mm^2)$	-	39	18	32	15	19
Error (x;y)		(1.0;1.2)		(1.3;1.2)		(2.4;2.1)
Embedded Lump	C_2					
$S(mm^2)$	-	-	-	35	-	31
Error (x;y)		(0.4;.2)		(1.5;1.2)		(0.3;1.4)
Embedded Lump	C_3					
$S(mm^2)$	-	-	-	-	-	22
Error (x;y)		(0.1;1.1)		(1.3;2.4)		(0.3;0.5)

Table 2: Position error and the resulting surface for the embedded spherical lumps is reported for Phantom 1.

Phantom 2						
Head Diameter	d_1		d_2		d_3	
Indentation Depth	$\delta = 3$	$\delta = 5$	$\delta = 3$	$\delta = 5$	$\delta = 3$	$\delta = 5$
Embedded Lump	A_1					
$S(mm^2)$	187	203	187	192	95	82
Error (x;y)		(0.4;.9)		(1.5;2.5)		(1.4;2.3)
Embedded Lump	A_2					
$S(mm^2)$	184	177	168	153	82	78
Error (x;y)		(1.4;2.1)		(0.4;.3)		(0.7;.4)
Embedded Lump	A_3					
$S(mm^2)$	172	165	144	147	94	103
Error (x;y)		(.4;1.3)		(1.4;1.2)		(2.3;1.2)
Embedded Lump	B_1					
$S(mm^2)$	141	144	124	127	95	81
Error (x;y)		(2.1;1.2)		(2.9;1.4)		(0.1;1.3)
Embedded Lump	B_2					
$S(mm^2)$	147	154	121	132	87	74
Error (x;y)		(2.6;1.2)		(1.5;1.4)		(2.5;3.1)
Embedded Lump	B_3					
$S(mm^2)$	138	141	107	115	69	81
Error (x;y)		(1.5;2.4)		(0.5;2.1)		(2.5;1.2)
Embedded Lump	C_1					
$S(mm^2)$	42	45	32	41	19	29
Error (x;y)		(1.7;1.5)		(0.3;1.4)		(2.4;1.5)
Embedded Lump	C_2					
$S(mm^2)$	28	34	27	35	14	24
Error (x;y)		(3.1;2.4)		(0.5;1.7)		(3.2;1.7)
Embedded Lump	C_3					
$S(mm^2)$	25	32	19	33	17	21
Error (x;y)		(2.1;1.5)		(3.3;.4)		(2.3;0.7)

Table 3: Position error and the resulting surface for the embedded spherical lumps is reported for Phantom 2.

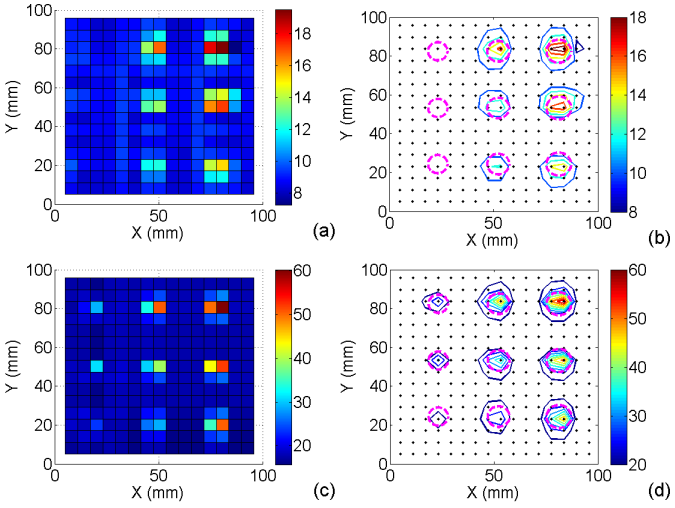

Figure 9: Pressure maps obtained respectively by palpating the hardest phantom, PH_1, with 3 mm (a) and 5 mm (b) indentation depth and the resulting contour maps (c) and (d) for the same indentation values.

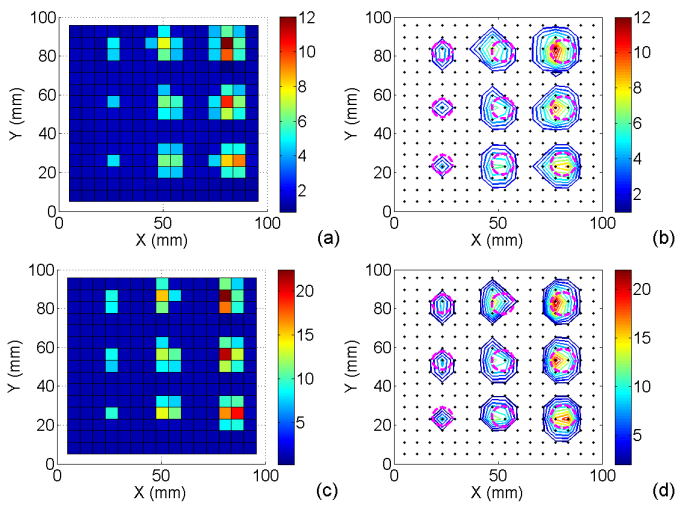

Figure 10: Pressure maps obtained respectively by palpating the softest phantom, PH_2, with 3 mm (a) and 5 mm (b) indentation depth and the resulting contour maps (c) and (d) for the same indentation values.

when palpation was performed with the d_1 spatial resolution, E_x=1.4 mm, E_y=1.6 mm for d_2 spatial resolution, and E_x=1.5 mm, E_y=1.5 mm for d_3 spatial resolution. The average area detected for 10 mm lumps A_1, A_2, and A_3 resulted in an average surface of 144 mm^2 when palpation was performed with d_1 (average relative error equal to 82.28 %), 133 mm^2 for d_2 (average relative error equal to 68.35 %), and 85 mm^2 for d_3 (average relative error equal to 7.6 %). The 8 mm lumps B_1, B_2, and B_3 resulted in average surfaces of $S_{d_1} = 104\ mm^2$ (average relative error 103 %), $S_{d_2} = 90\ mm^2$ (average relative error 80.7 %), and $S_{d_3} = 70\ mm^2$ (average relative error 40.5 %), respectively. Finally, the 6 mm lumps, C_1, C_2, and C_3, resulted in an average surface of $S_{d_1} = 35\ mm^2$ (average relative error 55.4 %), $S_{d_2} = 30\ mm^2$ (average relative error 39.9 %), and $S_{d_3} = 21\ mm^2$ (average relative error 25.4 %), respectively. The resulting average resulting lump detection success rate was equal to 86 % for d_1, 92 % for d_2, and 94.4 % for d_3, and by increasing δ to 5 mm, all lumps were detected, regardless of the head's diameter. The results suggest that the number of visible embedded lumps in the map increases with indentation depth, δ. Furthermore, the resulting evidence shows that lumps were detected more easily on the softest of the two phantoms (*i.e.*, PH_2). In fact, the trials on PH_1 confirmed that lumps C_2 and C_3 were never detected for the 3 mm indentation depth. Trials on PH_2, on the other hand, resulted on a 100 % detection rate for all lumps with both indentation depths.

The experiments suggest that the smallest diameter head (*i.e* d_3) is more effective in estimating the lump areas when compared to the larger diameter heads. The spatial distribution of the indentation points in our experimental set-up in fact depended on the actual diameter of the probe. The larger the diameter of the head, the larger the indentation point spacing, as well as the sensing area. Therefore, when palpating nearby the lumps at points along x and y, some lumps were perceived by the bigger heads, causing wider surface error. To overcome this problem and reduce the errors, a smaller spatial resolution can be adopted when indenting.

Palpation trials were thus repeated on PH_2 with d_1 and d_2 mounted on the WPP. For both heads, the indentation points were changed assuming palpation was performed with d_3 mounted, thus resulting in a smaller spatial resolution. Figure 11 shows the trials performed with d_1 on PH_1 for both the indentation depth. The average area detected by the two heads for the 10 mm lumps (A_1, A_2, and A_3) resulted in surface of 106 mm^2 (average relative error 36 %). The 8 mm lumps (B_1, B_2, and B_3) resulted in an average surface of 60.3 mm^2 (average relative error 20.4 %) and finally the 6 mm lumps, (C_1, C_2, and C_3), had an average surface of 31.4 mm^2 (average relative error 12 %). For both the head diameters, the resulting maps showed an average resulting lump detection rate equal to 94.4 % and the same ability to detect lumps as the smaller head. These results suggest that better lump detection can be achieved with the combination of greater indentation depth and smaller spatial resolution.

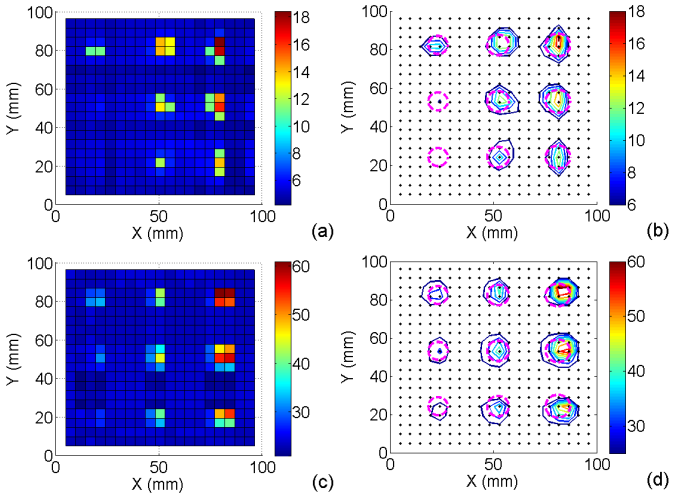

Figure 11: Pressure maps obtained respectively by palpating the hardest phantom with 3 mm (a) and 5 mm (b) indentation depth with the smaller spatial resolution. The resulting contour maps for the same indentation values: 3 mm (c) and 5 mm (d).

The palpation procedure performed took respectively 8 min and 26 s ± 1 s for d_1, 10 min and 41 s ± 1 s for d_2, and 13 min and 21 s ± 1 s for d_3 with the probe moved by the robotic manipulator. If we consider the case of a MIS procedure, where the probe is manipulated by a surgical grasper and the surgeon is assumed to palpate at a frequency of 0.5 Hz, the same area of the phantoms used in the benchtop trials would be covered in less than 10 m. This amount of time is a reasonable expectation for MIS surgery and is completely within the probe battery capacity.

6. Conclusions

In this work, a new calibration methodology was implemented for the WPP to reduce the error introduced by rubber nonlinearities on pressure measurements, thus enabling reconstruction of the measured pressure from the silicone rubber indentation. The method was validated with different diameter heads fabricated according to a new design that allows for exchangeability and disposability of the pressure sensing element. The bench-top experiments showed good repeatability and accuracy in quantitative measurements of different elastic moduli with a relative error below 3 %, regardless of the mounted head diameter. Furthermore, the device proved its ability to effectively detect different size lumps embedded into a silicone tissue simulator: the diameter of the head does not affect the device's ability in lump detection and there is no need for preoperative surface registration. Trials with the greater indentation depth demonstrated how buried lumps can be effectively detected without exceeding 6 N, a force value which can lead to tissue damage [23].

The identification of precise margins for curative resection, overall, showed an overestimated malignant area especially when the indentation points are not close to each other. However, during tissue resections, a clearance of at least 1 cm is recommended to prevent positive tumors margins [24]. As such, the overestimated area does not comport any disadvantage to the WPP usability in MIS, and it can considerably aid surgeons in procedures that involve the accurate targeting of malignant areas, both near the surface and further buried.

As such, future work will focus on increasing the probe's spatial resolution. The current embedded sensor package dimensions do not guarantee the fabrication of WPP head diameters smaller than 8 mm, limiting the maximum number of embedded sensors. Thus, a smaller package pressure sensor can be integrated (*e.g.*, BMP180, Bosh, USA) or triaxial force sensors can be explored as valid alternatives [25, 26]. The current calibration methodology requires the use of a reference force sensor to characterize the embedded sensor response. Analytical characterization of the silicone rubber's mechanical properties and geometry can substitute the calibration procedure by implementing techniques such as those presented in [27], to improve the sensor's spatial resolution and its ability to detect buried structures and further reduce the area of resected healthy tissue.

7. Acknowledgment

This work was supported by the National Science Foundation under Grant No.CNS-1239355.

8. References

[1] S. Phipps, T. Yang, F. Habib, R. Reuben, S. McNeill, Measurement of tissue mechanical characteristics to distinguish between benign and malignant prostatic disease, Urology 66 (2) (2005) 447–450.

[2] V. Jalkanen, B. M. Andersson, A. Bergh, B. Ljungberg, O. a. Lindahl, Prostate tissue stiffness as measured with a resonance sensor system: a study on silicone and human prostate tissue in vitro., Medical & biological engineering & computing 44 (7) (2006) 593–603.

[3] J. Fuller, W. Scott, B. Ashar, J. Corrado, Laparoscopic trocar injuries: A report from a U.S. Food and Drug Administration (FDA) Center for Devices and Radiological Health (CDRH) Systematic Technology Assessment of Medical Products (STAMP) committee, www.fda.gov/medicaldevices/safety/alertsandnotices/ucm197339.htm (2003).

[4] A. Cuschieri, Whither minimal access surgery: tribulations and expectations, The American Journal of Surgery 169 (1) (1995) 9–19.

[5] V. Velanovich, Laparoscopic vs open surgery, Surgical Endoscopy 14 (1) (2000) 16–21.

[6] J. C. Gwilliam, Z. Pezzementi, E. Jantho, A. M. Okamura, S. Hsiao, Human vs. robotic tactile sensing: Detecting lumps in soft tissue, 2010 IEEE Haptics Symposium (2010) 21–28.

[7] M. Tavakoli, R. Patel, M. Moallem, Robotic suturing forces in the presence of haptic feedback and sensory substitution, in: Control Applications, 2005. CCA 2005. Proceedings of 2005 IEEE Conference on, 2005, pp. 1–6.

[8] B. Demi, T. Ortmaier, U. Seibold, The touch and feel in minimally invasive surgery, in: Haptic Audio Visual Environments and their Applications, 2005. IEEE International Workshop on, 2005, pp. 33–38.

[9] M. Hashizume, M. Shimada, M. Tomikawa, Y. Ikeda, I. Takahashi, R. Abe, F. Koga, N. Gotoh, K. Konishi, S. Maehara, K. Sugimachi, Early experiences of endoscopic procedures in general surgery assisted by a computer-enhanced surgical system, Surgical Endoscopy And Other Interventional Techniques 16 (8) (2002) 1187–1191.

[10] P. Dario, M. Bergamasco, An advanced robot system for automated diagnostic tasks through palpation, Biomedical Engineering, IEEE Transactions on. 35 (2) (1988) 118–126.

[11] R. Howe, W. Peine, D. Kantarinis, J. Son, Remote palpation technology, IEEE Eng. Med. Biol. Mag. 14 (3) (1995) 318–323.

[12] P. Puangmali, K. Althoefer, L. D. Seneviratne, D. Murphy, P. Dasgupta, State-of-the-Art in Force and Tactile Sensing for Minimally Invasive Surgery, IEEE Sensors Journal 8 (4) (2008) 371–381.

[13] M. I. Tiwana, S. J. Redmond, N. H. Lovell, A review of tactile sensing tecnologies with applications in biomedical engineering, Sensors and Actuators A: Physical 179 (2012) 17–31.

[14] J. Engel, J. Chen, C. Liu, Development of polyimide flexible tactile sensor skin, Journal of Micromechanics and Microengineering 13 (2003) 359–366.

[15] M. Shimojo, Spatial filtering characteristic of elastic cover for tactile sensor, in: Robotics and Automation, 1994. Proceedings., 1994 IEEE International Conference on, 1994, pp. 287–292.

[16] S. Schostek, M. O. Schurr, G. F. Buess, Review on aspects of artificial tactile feedback in laparoscopic surgery., Medical engineering & physics 31 (8) (2009) 887–98.

[17] M. Beccani, C. Di Natali, L. Sliker, J. Schoen, M. Rentschler, P. Valdastri, Wireless tissue palpation for intraoperative detection of lumps in the soft tissue, Biomedical Engineering, IEEE Transactions on 61 (2) (2014) 353–361.

[18] Y. Tenzer, L. Jentoft, R. Howe, The feel of MEMS barometers: Inexpensive and easily customized tactile array sensors, Robotics Automation Magazine, IEEE 21 (3) (2014) 89–95.

[19] M. Beccani, C. Di Natali, N. E. Hall, C. E. Benjamin, C. S. Bell, P. Valdastri, Wireless Tissue Palpation: characterization of the probe head to improve detection of tumors in soft tissue, in: Eurosensors 2014, Brescia, Italia, in Procedia Engineering, in press., xxviii Edition, 2014.

[20] C. Di Natali, M. Beccani, P. Valdastri, Real-Time Pose Detection for Magnetic Medical Devices, IEEE Transactions on Magnetics 49 (7) (2013) 3524–3527.

[21] B. Libraries, http://www.boost.org, accessed on 23 October 2014.

[22] J. Rosen, J. D. Brown, S. De, M. Sinanan, B. Hannaford, Biomechanical properties of abdominal organs in vivo and postmortem under compression loads., Journal of biomechanical engineering 130 (2) (2008) 021020–5.

[23] M. T. Perri, A. L. Trejos, M. D. Naish, R. V. Patel, R. A. Malthaner, Initial evaluation of a tactile/kinesthetic force feedback system for minimally invasive tumor localization, Mechatronics, IEEE Transactions on. 15 (6) (2010) 925–931.

[24] A. Cucchetti, G. Ercolani, M. Cescon, E. Bigonzi, E. Peri, M. Ravaioli, A. D. Pinna, Impact of subcentimeter margin on outcome after hepatic resection for colorectal metastases: A meta-regression approach, Surgery 151 (5) (2012) 691–699.

[25] P. Valdastri, K. Harada, A. Menciassi, L. Beccai, C. Stefanini, M. Fujie, P. Dario, Integration of a miniaturised triaxial force sensor in a minimally invasive surgical tool, Biomedical Engineering, IEEE Transactions on. 53 (11) (2006) 2397–2400.

[26] Y. Hu, R. Katragadda, H. Tu, Q. Zheng, Y. Li, Y. Xu, Bioinspired 3-D tactile sensor for minimally invasive surgery, Journal of Microelectromechanical Systems 19 (6) (2010) 1400–1408.

[27] P. Wellman, R. Howe, Extracting features from tactile maps, in: Medical Image Computing and Computer-Assisted Intervention MICCAI99, Vol. 1679, 1999, pp. 1133–1142.